The 16p11.2 microdeletion influences how early-life microbiota perturbations affect hippocampal development and behavior throughout the lifespan

Courtney R. McDermott[1*], Zhan Gao[2], Anya S. Mirmajlesi[3], Christiana Ntim[4], Katherine Kimbark[5], Divya Thomas[4], Zain Mughal[4], Xue-Song Zhang[2], Xiaofeng Zhou[6], Daniel Popov[7], Alisa Halchenko[8], Jinchuan Xing[9], Smita Thakker-Varia[6], Janet Alder[6], James H. Millonig[2,6], Benjamin A. Samuels[9], Martin J. Blaser[2], Emanuel DiCicco-Bloom[6,11*]

[1] Mortimer B. Zuckerman Mind Brain and Behavior Institute, Columbia University, NY
[2] Center for Advanced Biotechnology and Medicine, Rutgers University, NJ
[3] Department of Rehabilitation Medicine, New York University Grossman School of Medicine, NY
[4] Department of Cell Biology & Neuroscience, Rutgers University, NJ
[5] Department of Neural & Behavioral Sciences, Penn State College of Medicine, PA
[6] Department of Neuroscience & Cell Biology, Rutgers Robert Wood Johnson Medical School, NJ
[7] Department of Biology, Rutgers University, NJ
[8] Department of Neuroscience, University of Vermont, VT
[9] Department of Genetics, Rutgers University, NJ
[10] Department of Psychology, Rutgers University, NJ
[11] Department of Pediatrics, Rutgers Robert Wood Johnson Medical School, NJ.

[*] Correspondence: crm2259@columbia.edu (CRM), diciccem@rwjms.rutgers.edu (EDB)

Abstract

Neurodevelopmental disorders result from interactions between genetic predisposition and environmental risk factors, with infancy being the most vulnerable period. We designed a longitudinal study to determine how short-term antibiotic exposure during early postnatal life impacts the gut microbiome, neurodevelopment, and behavior, and whether these alterations were exacerbated by the neurodevelopmental disorder-associated 16p11.2 microdeletion (16pDel) mutation. The cephalosporin antibiotic, cefdinir, broadly altered the gut microbiome acutely, with persistent reductions in several *Lachnospiraceae* genera despite overall recovery. These alterations preceded long-term behavioral changes, including reduced juvenile sociability, compromised risk assessment, and deficits in associative learning. Remarkably, only cefdinir-exposed 16pDel mice had changes in hippocampal stem cell proliferation, subsequent adolescent cell numbers, and gene expression compared to other groups, demonstrating that genetic predisposition can modulate the effects of early-life antibiotic exposure on neurodevelopment. These alterations may be mediated by gastrointestinal disturbances, as cefdinir-exposed 16pDel males had increased intestinal permeability and shifted metabolite profiles including arginine biosynthesis and glycerophospholipid metabolism. Taken together, this study highlights how early-life microbial alterations affect behavior and reveals that genetic predisposition influences antibiotic-induced changes in hippocampal development. Further, these insights identify metabolic mechanisms as potential targets for intervention and may raise concerns regarding antibiotic use during infancy.

Introduction

The average child in the United States receives more than two antibiotic courses by three years of age, which is often pre-emptive and unnecessary[1,2]. This over- and misuse during critical developmental periods has been linked to adverse health outcomes, including neurodevelopmental disorders (NDDs)[3–6]. For example, birth cohort studies have shown associations of antibiotic exposure during early life with increased risks of attention deficit hyperactivity disorder and autism spectrum disorder risk (ASD)[4–6]. Our recent study of 14,572 children found that cephalosporin exposure in the first two years of life was associated with increased ASD risk in males and females (hazard ratios 1.89 and 2.77, respectively)[3]. Although these studies reflect association and not causation, they warrant investigation of causal factors and underlying mechanisms connecting early-life antibiotic use to NDD outcomes.

Accumulating evidence suggests that the gut microbiome is a nexus in the link between antibiotic exposure and NDDs[7–11]. Studies in both humans and experimental animals have shown that antibiotic exposure disrupts homeostasis within the gut microbiome, as indicated by altered bacterial richness and population structure[12–14]. Such alterations, particularly in early life, may impact nervous system development through the gut microbiome-brain axis, acting via the vagus nerve and metabolic, endocrine, and immune mediating pathways[15–17]. However, current research on neural and behavioral alterations following antibiotic exposure has primarily focused on the adult brain, overlooking the sensitive neurodevelopmental timeframe when neural populations underlying connectivity are established[8,10,18,19]. Furthermore, most studies have used prolonged, high-dose antibiotic regimens to suppress the microbiome, an approach that doesn't reflect typical

clinical pediatric practice[8,10,19–23]. To address these gaps, we utilized a short-term, therapeutic dose of a cephalosporin antibiotic during early life and characterized changes in fundamental neurodevelopmental processes.

In the postnatal rodent brain, neural stem cell (NSC) proliferation peaks in the hippocampal dentate gyrus during the first two weeks of life[24]. These NSCs give rise to intermediate progenitor cells that undergo frequent mitotic cell divisions before migrating and differentiating into neurons or astrocytes[25]. Given NSCs' implications in NDD pathogenesis and sensitivity to genetic and environmental factors, we investigated how early-life antibiotic-induced microbiome alterations affect hippocampal NSC proliferation, an understudied area[26–29]. Additionally, while antibiotics may impact neurodevelopment, not all exposed infants go on to develop a NDD, highlighting the potential role of genetic predisposition. To examine this issue, we used both wildtype (WT) and 16p11.2 microdeletion copy number variation (16pDel CNV) mice in this study. The 16pDel CNV mouse has been well-characterized, and exhibits alterations in angiogenesis, corticogenesis, basal ganglia volume, ERK signaling, metabolism, and behavior[30–36]. This CNV is a robust genetic mutation for experimentation, as approximately 30% of humans with the 16p CNV (deletion + duplication) receive an ASD diagnosis, accounting for ~1% of total ASD cases, while essentially all display a NDD[37–40]. Furthermore, since individuals with this deletion display altered metabolic profiles, they may be particularly vulnerable to biochemical alterations that accompany microbiome perturbations from antibiotic exposure[41,42].

Here, we investigate how a short-term therapeutic dose of a cephalosporin antibiotic during early life affects gut microbiome composition, metabolites, hippocampal development, and behavior. We show that this conservative regimen perturbs the gut microbiome and induces NDD-related behaviors. Notably, only cephalosporin-exposed 16pDel mice exhibited altered hippocampal development, highlighting the influence of genetic predisposition on the effects of early-life antibiotic exposure.

Results

A brief therapeutic exposure to cefdinir during early life perturbs the gut microbiome

Litters comprised of WT and 16pDel mice were randomly assigned to receive saline (control) or 10mg/kg cefdinir via gavage from postnatal (P) days 5-9 (**Fig1A**, detailed sample sizes in **Supplementary file 1**). We used 16S rRNA gene sequencing to profile microbial composition changes across the intestinal tract during the pre-weaning or weaning period (P13 and P21, respectively). At P13, all cefdinir-exposed mice had shifts in microbial community structure (β-diversity) in the cecum compared to saline-exposed groups, indicated by both Jaccard and Bray-Curtis distances (**Fig 1B, S1A**), with parallel findings in the colon (**FigS1B-C**), and ileum (**FigS1D-E**). Differences in β-diversity ($p<0.05$) were also detected when comparing saline-exposed WT and 16pDel males, but not females. The broad cefdinir-induced β-diversity alterations were accompanied by reductions in bacterial richness (α-diversity) within the cecum and colon (**Fig1C, S1F)**, but not the ileum (**FigS1G**). These shifts were not due to changes in total bacterial abundance (**Fig 1D**). The bacterial taxa underlying these changes at the genus level were assessed using the Microbiome Multivariate Association with Linear Models 2 (MaAsLin2)

R package[43] (**Fig1E**). There were significant reductions in the cecum of all cefdinir-exposed mice of most major taxa, including *Streptococcaceae*, *Lachnospiraceae* and *Ruminococcaceae*, with elevated abundance of *Enterococcaceae*. Similar results were observed in the colon and ileum (**FigS1H-I**). The cefdinir-induced microbial changes are not likely the consequence of differences in nursing, as neither the weight of the milk-containing stomach nor the body differed at P11 and P13, respectively **(FigS1J-K).** At P21, although α-diversity in cefdinir-exposed mice no longer differed from saline controls (**Fig1F, S2A-B**), the shifts in β-diversity persisted within the cecum, colon, and ileum (**Fig1G, FigS2 A-D**). In similar fashion, several *Lachnospiraceae* and *Ruminococcaceae* genera continued to be reduced in cecal samples of P21 cefdinir-exposed mice (**Fig1H**), changes that persisted throughout the lifespan, as reflected in fecal specimens at P21 to P80 (**FigS3A-D**). Despite these specific taxonomic changes, overall α- and β-diversity indices were comparable between saline- and cefdinir-exposed fecal specimens at P21 to P80 (**FigS4A-H**). This suggests that while certain bacterial groups were affected, the overall community structure and diversity were maintained in fecal samples, highlighting the complex dynamics of microbial ecosystems in response to antibiotic exposure.

Cefdinir-exposed mice display altered behavior throughout the lifespan

We next investigated whether microbiome perturbations in early life would produce behavioral features related to NDDs (**Fig2A**). Since we did not observe any sex differences in our initial behavioral analyses, results for the sexes are combined. At P21, immediately prior to weaning, cefdinir-exposed mice showed reduced engagement with a novel sex- and age-matched mouse compared to saline-exposed mice, which was

driven by the 16pDel group (**Fig2B**). All mice had similar levels of social odor detection and discrimination, suggesting that the observed social differences were not attributable to altered olfactory perception (**Fig2C**). In contrast, cefdinir-exposed mice displayed increased social preference during adulthood, but no changes in social novelty preference (**Fig2D, FigS5A**). We also observed reduced risk-aversion responses in the elevated plus maze at P63 and impaired associative learning in the contextual fear conditioning task P89 in cefdinir-exposed mice (**Fig2E-G**). We did not detect alterations in the novel object recognition task or in the marble burying task across treatment or genotype comparisons (**FigS5B-C**). In subsequent analyses, saline-exposed 16pDel mice showed less exploratory behavior compared to WT littermates (**FigS5D).** This was accompanied by decreased distance traveled in the center arena and less time spent there, along with increased time in the periphery (**FigS5E-G**). Collectively, these studies demonstrate that early-life cefdinir-induced microbiome perturbations result in long-term NDD-associated behavioral changes in adulthood.

Genetic susceptibility impacts hippocampal alterations associated with an antibiotic-induced perturbed microbiome

To determine if the cefdinir-induced behavioral changes were associated with altered neurodevelopment, we investigated neurogenesis and astrogenesis in the hippocampus, a brain region critical for learning and memory and associated with NDD-related behaviors[26,44,45]. Four days after antibiotic cessation (P13), cefdinir-exposed 16pDel males showed a robust decrease in cell cycle regulator, Cyclin E, while 16pDel females exhibited an increase (**Fig3A**). No changes were observed in WT male or female mice.

Remarkably, we detected parallel reductions in Ki67$^+$ and EdU$^+$ NSCs in cefdinir-exposed 16pDel males at P13, and a trending decrease in Sox9$^+$ astrocytes at P21 (**Fig3B-D**). In contrast, cefdinir-exposed 16pDel females showed no changes in Ki67$^+$ and EdU$^+$ NSCs at P13 but had a 53% increase in Prox1$^+$ granule neurons at P21, indicating temporal and sex-specific differences in the responses (**Fig3A-B, E**). We do not suspect these alterations were due to either increased blood brain barrier permeability or apoptosis, or from the antibiotic itself, since our pilot studies revealed comparable results between saline-exposed and cefdinir-exposed mice (**FigS6A-D).** Further, while microbiome disturbances may impact inflammatory pathways, early-life cefdinir exposure did not alter Iba1$^+$ microglial cell numbers in the hilus at P21 (**FigS6E**), though changes in microglial activation and cytokines remain to be defined.

Transcriptional changes in cefdinir-exposed 16pDel males overlap with autism-associated genes

The robust 16pDel responses in our neurodevelopmental analyses prompted us to profile changes in hippocampal transcript levels to identify genes and pathways that may underlie this unique gene-environment phenotype. For these studies, we performed bulk RNA sequencing on hippocampal tissues from a subset of P13 and P21 mice used concurrently for our microbiome and immunoblotting analyses, enabling us to assess temporal regulation of transcriptional changes. First, we confirmed correct expression of sex-determining genes in females and males, and the expected reduced expression of the 16p11.2 interval genes in 16pDel mice (**FigS7A-D**). At P13, there were no significant differentially expressed genes (DEGs) between all cefdinir- and saline-exposed mice

(**Fig4A**), or within the WT female and male subgroups (**Fig4B-C**). However, at P13, we observed 5 DEGs in cefdinir-exposed 16pDel females and 118 DEGs in 16pDel males compared to saline-exposed 16pDel controls (**Fig4D-E**). The 118 DEGs in cefdinir-exposed 16pDel males overlapped with curated lists of high-confidence ASD risk genes (**Fig4F**). Nine overlapped with the SFARI database[46], and four overlapped with the ASC database[47], with *Hdac4* and *Cadm1* appearing in both.

At P21, we identified 2 DEGs when comparing all cefdinir- vs saline-exposed mice, 130 in WT females, 190 DEGs in WT males, 22 in 16pDel females, and 261 in 16pDel males (**Fig4G-K**). Despite the presence of DEGs across all groups at P21, only the 16pDel males showed significant differences in gene ontology (GO) pathways (**Supplementary file 2).** We detected overrepresented terms for myelination, glial cell development, and neurogenesis in the 108/261 upregulated DEGs, and terms for axonogenesis, neurogenesis, cell-cell adhesion, and vesicle-mediated transport in the 153/261 downregulated DEG set. The detection of three-fold differential expression of >1000 genes in both up- and downregulated datasets in neurogenesis may suggest how this expansive process is dynamically dysregulated in response to early-life cefdinir exposure. Importantly, these differences were not due to litter effects, as all mice in each group were taken from separate litters. These DEGs also overlapped with the ASD databases: 28 with SFARI, 18 with ASC, and 8 in both (**Fig4L**). Taken together, these expression data corroborate our developmental analyses, demonstrating that cefdinir-exposed 16pDel mice exhibit a unique vulnerability to early-life cefdinir exposure.

Cefdinir-exposed 16pDel mice display altered intestinal permeability, metabolites, and lipids

Given this observed vulnerability, we hypothesized that the 16pDel risk variant creates a susceptibility that, when combined with early-life cefdinir exposure, induces a leaky gut, leading to abnormal lipid and metabolite levels that may alter hippocampal development. To test this, we examined intestinal permeability and circulating metabolite and lipid profiles within saline- and cefdinir-exposed mice. There was a 3-fold increase in intestinal permeability as revealed by peripheral serum levels of gavaged FITC-dextran in cefdinir-exposed 16pDel males compared to saline-exposed 16pDel males at P11, a timepoint between antibiotic cessation (P9) and initial brain changes observed (P13) (**Fig5A-B**). No changes were detected in other groups. In targeted analysis of sera samples from mice at P13, all cefdinir-exposed mice had reduced levels of pyruvate, N,N-dimethylglycine, N-acetylglycine, 2-hydroxybutyrate, and cytosine, with the latter four driven by the 16pDel group (**Fig5C-G**). Decreases in cholesterol ester and sterol content were also observed exclusively in cefdinir-exposed 16pDel mice (**Fig5H-I**). To identify metabolic pathways that may underlie these unique changes, we analyzed 29 metabolites that were correlated with cholesterol ester content in cefdinir-exposed 16pDel mice using the MetaboAnalyst KEGG database (**Fig5J**)[48]. This analysis revealed alterations in arginine biosynthesis and glycerophospholipid metabolism as significantly altered pathways, which is consistent with their known roles in neural physiology and disease (**Fig5K**)[49–53]. By P21, most of the P13 lipid differences subsided; however, five new metabolites (5-hydroxylysine, nicotinamide adenine dinucleotide, glycine, sorbitol, and creatinine) were reduced in all cefdinir-exposed mice indicating that the metabolic effects of cefdinir

exposure were dynamic (**Fig5L**). In total, these findings indicate there are genotype-specific intestinal and metabolic responses that may modulate the effects of early-life cefdinir exposure on neurodevelopment.

Discussion

We designed an animal study that modeled therapeutic antibiotic exposure in human infants to investigate how its impact on the gut microbiome affects hippocampal development and behavior. This research has significant implications for childhood development, as both clinical and epidemiological studies provide evidence that the widespread use of antibiotics during infancy may increase susceptibility to adverse health outcomes and neuropsychiatric conditions[2–6,54,55]. The most substantial microbial alterations were detected 4 days after antibiotic cessation (P13), with signs of recovery by P21, most likely due to diminished antibiotic levels as well as the transition to solid food consumption. However, we discovered an unexpected long term-effect: several genera within the *Lachnospiraceae* family remained at reduced levels throughout the lifespan of cefdinir-exposed mice. Other studies of antibiotic-exposed infants and mature rodents have demonstrated depleted *Lachnospiraceae* to be associated with a less developed intestinal microbiome, disrupted metabolism, and alterations in neural development or function[55–58]. Whether the antibiotic effects on behavior reflect the initial neurodevelopmental changes or the continued microbiome disruption, or the combination of both, remains to be determined.

Remarkably, mice exposed to cefdinir during early life showed NDD-related behavior changes across multiple domains, even two months after antibiotic cessation. Leclercq *et*

al., (2017) are among the few to also use a single antibiotic during early life and show corresponding changes in behavior[11]. In their model, 4 weeks of penicillin V exposure from E12-P21 resulted in decreased social preference and impaired risk-aversion behaviors around P42. Similarly, our conservative 5-day exposure during early life also led to altered social behavior, although results across measures were mixed. The unexpected increase in social preference by P80 can be interpreted as an adaptive response or arises from the methodological differences between the two tasks. In the P21 sociability task, the experimental mouse was confined to a small home cage with a freely moving novel mouse. In contrast, at P80, the mouse was placed in a chamber ~3x the size of a home cage with the choice to engage with a novel mouse enclosed in a wire cup. The larger testing environment at P80 may have allowed for a more nuanced expression of social behavior, potentially revealing aspects of social interaction that were masked in the more confined setting at P21. Nevertheless, cefdinir-exposed mice displayed alterations in the elevated plus maze and contextual fear conditioning tasks, consistent with previous studies[21,59]. At P60, cefdinir-exposed mice spent more time in the open arms of the elevated plus maze, suggesting a reduction in innate risk-avoidance behaviors, as mice typically prefer enclosed spaces for safety. This result aligns with Leclercq *et al*., (2017), in which male mice exposed to penicillin V spent more time in the open arms[11]. Finally, we observed reduced extinction learning in cefdinir-exposed mice at P89, nearly three months after initial antibiotic exposure. This long-term effect aligns with findings by Chu *et al*., (2019), who showed reduced extinction learning in adult mice treated with a prolonged mixture of broad-spectrum antibiotics[21]. The reproducible evidence of antibiotic exposure in mice eliciting compromised fear-aversion behaviors

and extinction learning suggest that the microbiota may play a substantial role in modulating these behaviors, even after a brief exposure consistent with common therapeutic regimens.

While cefdinir exposure induced changes in the gut microbiome and behavior across all groups, our analysis of hippocampal development revealed effects that varied depending on genotype and sex. Cefdinir-exposed 16pDel males exhibited reductions in hippocampal NSC proliferation and astrocyte numbers, while cefdinir-exposed 16pDel females exhibited increased Cyclin E protein and granule neurons. The increased numbers of Prox1^{+} neurons in cefdinir-exposed 16pDel females may arise from altered cell cycle dynamics, consistent with the absence of changes in Ki67^{+} and EdU^{+} NSCs at P13. To investigate a potential slower cell cycle in females at P13 following cefdinir exposure, future studies should employ EdU and IdU at multiple intervals to determine cell cycle lengths of different cell populations[28,60–62]. While a change in microglial cell numbers may have been expected, its absence could be due to our relatively low dose and short timeframe of cefdinir exposure, which may attenuate an immune response triggered by the perturbed gut microbiome. Further, changes in microglia may have occurred at the cell activation level, which this study did not assess. Future studies should quantify the expression of activated microglia (CD68) and both pro- and anti-inflammatory cytokines.

This unique gene-environment effect was further corroborated by our hippocampal bulk RNA sequencing data. Significantly, a proportion of DEGs in cefdinir-exposed 16pDel

males overlapped with curated lists of high-risk ASD genes, providing initial evidence that genetic constitution may influence how early-life cefdinir exposure contributes to ASD occurrence. Similar to a recent study by Kim *et al*., (2024), we detected downregulation of ribosomal genes in our 16pDel males, but only after cefdinir exposure[33]. The inconsistency in observing this result at baseline may be attributed to differences in the brain region analyzed (hippocampus vs striatum) and age at comparison (P13 vs ~P70-112). Interestingly, *Hdac4* and *Cadm1* were 2 of the 118 cefdinir-exposed 16pDel DEGs that overlapped with both the SFARI and ASC human ASD risk gene databases[46,47]. Both *Hdac4* and *Cadm1* play substantial roles in cell cycle progression; *Hdac4* is a histone deacetylase that removes acetyl groups from histones which condenses chromatin and represses transcription, while CADM1 is a cell adhesion molecule that regulates several signaling pathways, including AKT, EMT, and STAT3[63,64]. Elevated levels of *Hdac4* and *Cadm1* individually inhibit cell cycle progression, potentially contributing to the reduced NSC proliferation phenotype in this group[64]. Despite detection of DEGs in all groups at P21, only the 261 DEG set in 16pDel males yielded GO terms that met an FDR<0.05 cutoff value, further underscoring that genotype and sex influence neural alterations following early-life cefdinir exposure.

To define potential mechanisms underlying the unique neural phenotype in cefdinir-exposed 16pDel mice, we investigated intestinal permeability and profiled peripheral lipids and metabolites. While we observed increased intestinal permeability in cefdinir-exposed 16pDel males, future studies examining epithelial tight junction proteins are needed to identify the precise location and nature of the gut barrier disruption. Further,

levels of cholesterol esters and sterols were selectively reduced in cefdinir-exposed 16pDel mice, consistent with clinical observations in a subset of individuals with NDDs[65]. These reductions may impact neurodevelopment, given the role of cholesterol metabolites in synapse formation, membrane trafficking, and neural signaling, and functions of sterols in maintaining neuronal membrane integrity and serving as precursors for neurosteroids, which modulate neurotransmitter activity[66,67]. Further, identified metabolites involved in arginine biosynthesis and glycerophospholipid metabolism were uniquely altered in cefdinir-exposed 16pDel mice. Individuals with the 16p11.2 deletion exhibit disrupted metabolism and obesity[68,69]. Metabolic alterations induced by a disturbed microbiome may synergize with this genetic mutation, potentially representing a mechanism through which early-life cefdinir exposure interacts with genetic predisposition to influence hippocampal development[68,69]. Arginine is a precursor for nitric oxide synthesis, which is essential for neurovascular function and synaptic plasticity[70,71]. Notably, the 16pDel mouse exhibits abnormalities in neurovascular formation and function[35]. Glycerophospholipid metabolism, another key pathway identified in our analysis, is fundamental to brain health and function. Glycerophospholipids are major constituents of neural membranes and serve as reservoirs for second messengers involved in neural signaling[72]. Disruptions in glycerophospholipid metabolism have been linked to microbiota dysbiosis, as evidenced by altered glycerophospholipid profiles in hippocampus of germ free female cynomolgus macaques and mouse prefrontal cortex[73,74]. Finally, it is notable that changes in cholesterols, sterols, and metabolites were limited to the P13 timepoint, while recovery was apparent by P21, suggesting that neurodevelopmental alterations were already established before weaning.

In summary, our gene-environment experimental design revealed that male mice harboring the 16pDel are uniquely vulnerable to cefdinir-induced changes in hippocampal development and identified potential metabolic mechanisms as targets for intervention. These findings underscore the importance of considering genetic predisposition and sex when evaluating the potential neurodevelopmental impacts of pediatric antibiotic treatment, which could inform the development of more targeted interventions or protective strategies in clinical practice for vulnerable populations.

Methods

Ethical statement

All experimental protocols were conducted in compliance with NIH laboratory animal care guidelines and approved by the Rutgers University Institutional Animal Care and Use Committee (IACUC #PROTO999900063).

Mouse husbandry

Heterozygous 16p11.2$^{+/-}$ microdeletion (16pDel) male mice were purchased from The Jackson Laboratory (stock #013128; mixed B6/129 background). This line is maintained by breeding 16pDel males to B6129SF1/J “wildtype” (WT) females (stock #101043). The resulting litters are comprised of ~50:50 WT and 16pDel offspring. All mice were maintained on a 12 light:12 dark schedule where the lights were on from 6:00 a.m. to 6:00 p.m. Mice were housed in standard plastic cages in a colony room maintained at approximately 20°C, with ad libitum access to food and water.

Genotyping

Mice were genotyped by PCR analysis of tail DNA using standard PCR methods provided by Jackson Laboratories. 0.5 cm tail snips were digested using a Extracta™ DNA Prep for PCR-Tissue (Quantabio). The following primers were utilized in the PCR reaction for 16pDel: WT forward CCTGAGCCTCTTGAGTGTCC, WT reverse GTCGGTTCAGGTGGTAGACG, 16pDel forward ACCTGGTATTGAATGCTTGC, 16pDel reverse TGGTATCTCCATAAGACAGAATGC. These primers amplify a 194-bp band in WT and 16pDel mice, and a 369-bp band only in 16pDel mice. To confirm the sex of the mice, the following primers were used: SRY forward TTGTCTAGAGAGCATGGAGGGCCATGTCAA and SRY reverse CCACTCCTCTGTGACACTTTAGCCCTCCGA. A 273-bp band only appears for male mice.

Antibiotic Treatment

These studies used the cephalosporin antibiotic, cefdinir (Alfa Aesar). Cefdinir was prepared by dissolving the powder in 0.007% of 1N NaOH saline. Control-treated mice were exposed to the same 0.007% NaOH saline solution. Litters were randomly assigned to receive saline or 10mg/kg cefdinir via oral gavage on P5-9. Mice were weighted immediately prior to gavage to calculate volume administration.

Microbiome sample collection and processing

Offspring were sacrificed on P13 or P21, and the cecum, colon, and ileum were collected in cryopreservative tubes, snap frozen on dry ice, and stored at -80°C. Microbiota DNA

was extracted using the PowerSoil-htp 96-Well DNA Isolation Kit (Qiagen). The V4 region of bacterial 16S rRNA genes was amplified in triplicate reactions using barcoded fusion primers 515F/806R, which amplifies bacterial and archaeal 16S genes. The DNA concentration of the V4 amplicons for each sample was measured using the Quant-iT PicoGreen dsDNA assay kit (Life Technologies) and samples were pooled in equal quantities. These pools were treated with the Qiaquick PCR purification kit (Qiagen) to remove primers, quantified using the high-sensitivity dsDNA assay kit and the Qubit 2.0 Fluorometer (Life Technologies), and then combined at equal concentrations to form the sequencing library. The ~254-bp V4 region was sequenced using the IluminaMiSeq 2x150 bp platform at Azenta Life Sciences (South Plainfield, NJ). These procedures were also performed on fecal pellet samples at P21, P45, P60, and P80 of mice used in behavioral studies.

16S rRNA sequencing analysis

Quantitative insights for microbial ecology 2 (QIIME)[75] was used for quality filtering and downstream analysis for α-diversity, β-diversity, and compositional analysis. Sequences were filtered for quality, trimmed, de-noised, merged, and then the chimeric sequences were removed using DADA2[76] to generate the feature table. The Shannon index was used as a measure of α-diversity. β-diversity was computed as Jaccard distance matrix and Bray Curtis matrix, and differences in β-diversity were visualized with principal coordinate analysis plots. Taxonomy was assigned using SILVA[77]. Differential features of relative abundance of bacterial taxa were identified using the Microbiome multivariate association with linear models (MaAsLin2) algorithm[43].

Immunoblotting

Equal protein concentrations (35µg/lane) of P13 or P21 hippocampal lysates or P11 whole brain lysates were loaded on 12% acrylamide gels, blocked with 5% milk made in 0.05% triton-X tris-buffered saline, and incubated with primary antibody overnight at 4°C. Incubations with HRP-conjugated secondary antibody (1:1000; NA931V or NA934V, GE Healthcare) were performed for 1hr at room temperature and visualization was performed by chemiluminescence (ECL; GE Healthcare). Dilutions of primary antibodies were as follows: anti-Cyclin E (1:300; sc-377100, Santa Cruz), anti-cleaved caspase-3 (1:1000; 9664S, Cell Signaling) anti-occludin (1:1000, 40-4700, abcam) and anti-GAPDH (1:10,000; 60004-1-Ig, Proteintech). Bands were normalized to GAPDH and quantified using densitometry.

EdU administration and cryopreservation

In separate studies, P6 and P13 offspring were injected subcutaneously with 100mg/kg 5-ethynyl-2'-deoxyuridine (EdU; E10187, Invitrogen) to measure precursor S-phase entry. The EdU solution was made fresh on day of injection and prepared by dissolving the powder in a 0.007% of 1N NaOH saline solution. After 2hrs, animals were anesthetized, perfused with 0.1 mol/L (1X) PBS, followed by ice cold, fresh, 4% PFA (pH 7.40). Brains were post-fixed in 4% PFA for 24hrs at 4°C, cryoprotected in 30% sucrose, embedded in Tissue-Tek (Sakura), and stored at -80°C until day of cryosectioning.

Brain tissue processing

The left hemisphere of P6 and P13 mice were sectioned into 14-µm thick sagittal sections on a cryostat (Leica, Heidelberg, Germany). Every other tissue section was collected and mounted onto charged, uncoated slides (VWR Superfrost Plus Precleaned Microslides). For P21 stereological studies, brains were sectioned into 30-µm thick sagittal sections on a cryostat in a 1:10 series fashion.

Immunohistochemistry

Slides were washed with 1X PBS to remove OCT. Antigen retrieval was performed by incubating sections in boiling 0.01 mol/L citrate buffer for 10mins at 100°C, followed by gradual decrease in temperature between 82 and 85°C for another 10mins. Sections were then blocked with 33% normal goat serum (NGS)-0.5% Triton X-100 for 1hr at room temperature (RT), followed by Ki67 primary antibody (1:200; 5556003, BD Pharmigen) in 2% NGS-0.3% Triton X-100 overnight at 4°C. The next day, primary was washed off, and sections were incubated with goat anti-mouse 594 or goat anti-rabbit 488 secondary antibody (1:500; A11005, A11008 Invitrogen) for 1hr at RT. Sections were then counterstained with DAPI-PBS (1:1000; D21490, Invitrogen) at RT for 10mins before being washed with 1X PBS and coverslipped.

Click-iT EdU

Slides were washed with 1X PBS to remove OCT. Sections were then incubated with 0.5% Triton X-100 for 10mins, followed by two 5min washes with 3% BSA-PBS for blocking. The EdU staining solution was prepared as follows (for 1mL solution): 860µl 1x

Tris-HCl (pH 8.6), 40µl 100 mM CuSO4 (stock 16 mg/ml in H_2O; C495-500, Fisher Scientific), 2.5µl Alexa fluor azide (A10270, Thermo Fisher Scientific) and 100µl reaction buffer additive (Ascorbic acid, 200 mg/ml H_2O; A92902, Millipore Sigma). The sections were incubated with the EdU staining solution at RT for 30mins. Sections were then washed once more with 3% BSA-PBS, counterstained with DAPI (1:1000) for 10mins, and then coverslipped.

Cell quantification

Sections were visualized on an Axiovert 200M microscope (Zeiss, USA). Total numbers of EdU^+ and $Ki67^+$ cells in P6 and P13 offspring were counted in the hilus and subgranular zone of the hippocampal dentate gyrus on 40X and 20X, respectively. Quantification of EdU^+ and $Ki67^+$ cells at P13 were performed on an average of 8 sections/mouse, 3-6 mice/group, across 4 litters/treatment. Quantifications for P6 16pDel males were performed on an average of 6 sections/mouse, 3-4 mice/group, across 2 litters/treatment. Total numbers of $Iba1^+$ cells in P21 offspring counted in the hilus at 40x were performed on an average of 8 sections/mouse, 4-6 mice/group, across 4 litters/treatment. Data were collected blinded to treatment, sex, and genotype.

Stereological analysis

Sections were visualized on a ZEISS Axio Imager M2 microscope using Stereo Investigator (mbf BioScience). We used the optical fractionator workflow, with parameters set to a counting frame of x:15 y:15, a grid size of x:47 y:47, and 10% sampling of each outlined section. Brains with less than five viable sections were excluded from analyses.

A section that was not viable may have contained a slice of the brain that was too lateral, too medial, cut, folded, or that did not contain a dentate gyrus. The z-axis of the brain was measured and recorded for population calculation. Data was used from brain sections whose calculated cell population had a Gunderson m=1 coefficient error <0.1. Quantification was performed blind to genotype, sex, and treatment on every 10th section through the entire hippocampus. Total numbers of Prox1^{+} cells were quantified in the granule cell layer of the dentate gyrus. The granule cell layer was outlined on 10x and nuclei were counted under 63x oil. Total numbers of Sox9^{+} cells were quantified in the subgranular zone of the dentate gyrus. Total numbers of Iba1^{+} cells were quantified in the hilus. These studies were performed on an average of 5-9 sections/animal, 4-6 animals/group, across 4 litters/treatment.

Intestinal permeability

On P11, offspring were fasted 4hrs before gavage of 0.6 g/kg 4-kDa FITC-dextran (46944, Millipore Sigma). An additional 4hrs later, offspring were anesthetized, and serum was collected and assessed for fluorescence intensity (485 excitation, 528 emission) on the SpectraMax iD3 (Molecular Devices). The standard curve ranged from 0-12.8mg/mL, with 1:2 serial dilutions in saline. Sera from a non-FITC gavaged mouse (control) and all experimental mice were diluted 1:20 in saline. All standards and samples were assayed in triplicate wells on a 96-well plate.

Serum lipidomics and metabolomics

Blood was collected from mice used in the P13 and P21 microbiome studies. Samples were centrifuged at 5,000 RPM for 10mins at 4°C to obtain serum, which was then stored at -80°C until processing. Sera samples were extracted for lipids and polar metabolites using positive and negative ionization modes at the Metabolomics Shared Resource (MSR) of Rutgers Cancer Institute of NJ[78–82]. Lipids were annotated by MS-DIAL based on in silico databases. A Q Exactive Quadrupole-Orbitrap mass spectrometer coupled to Vanquish Horizon UHPLC system was used to acquire data in an untargeted manner. The MSR in-house database covers >400 polar metabolites with defined retention time and accurate mass.

Bulk RNA sequencing

The hippocampus was dissected from a subset of mice used in the P13 and P21 microbiome and metabolome studies. One hemisphere of each hippocampus was randomly saved for protein analyses, while the remaining hemisphere was immediately stored in RNAlater (Thermofisher) solution at 4°C for 24hrs, followed by removal of solution, and rapid storage of tissue at -80°C. The hippocampi were dissected using micro forceps and a dissecting microscope using landmarks from the Allen Institute Developing Mouse Brain Atlas[83]. For gene expression studies, RNA isolation, quality control, and mRNA sequencing was performed at Azenta Life Sciences. RNA integrity number values ranged from 6.1-9.6. The samples were sequenced using the IluminaHiSeq 2x150 bp platform. Sequence reads were trimmed using Trimmomatic v.0.36, which were then mapped to the *Mus musculus* GRCm38 reference genome available on ENSEMBL using

the STAR aligner v.2.5.2b. Unique gene hit counts within the exon regions were calculated using featureCounts from the Subread package v.1.5.2.

Juvenile social interaction

Juvenile reciprocal social interactions were tested on day 21 of age, immediately prior to weaning. The test was conducted in a sterile home cage covered with 0.5cm layer of clean bedding. Each subject mouse was singly housed in a clean cage for 1hr before the test. After this brief isolation period, the freely moving subject mouse and a freely moving age- and sex-matched C57BL/6J partner mouse were simultaneously placed in the arena and their interactions were videotaped for 10mins. Videos were scored blinded to treatment, genotype, and sex. Parameters of social behaviors included nose-to-nose sniff, front approach, nose-to-anogenital sniff. All behaviors were analyzed for frequency of occurrence.

Odor habituation/discrimination task

On P45, each experimental mouse was placed in a clean home cage and then exposed to various odors via saturated cotton swabs after 1hr of isolation. The task consisted of fifteen consecutive 1min trials: 3 trials with plain tap water, 3 trials with of 1:100 diluted vanilla extract (McCormick®), 3 trials with 1:00 diluted banana extract (McCormick®), 3 trials with social odor from 129/SvlmJ mice, and 3 trials with social odor from C57BL/6J mice. Social odor stimuli were prepared by wiping a swab in a zig-zag motion across a soiled cage of unfamiliar mice of the same sex. Time spent sniffing the swab was live

recorded with a stopwatch by an observer sitting 2m away from the testing cage, blinded to treatment and genotype. Sniffing was scored when the nose is within 1cm of the swab.

Open field exploration

Mice were exposed to a novel arena for 30mins in dim (100 lux) lighting on P60. Movement and location were measured by infrared beam breaks and analyzed with Kinder Scientific software. Rearing events, distance traveled, entries, and time in each compartment (center, periphery, and total) were analyzed.

Elevated plus maze

On P63, mice were placed in the elevated plus maze task to assess risk-avoidance behaviors. The test mouse was placed in the center of the chamber and allowed to freely explore the apparatus for 10mins. All sessions were video recorded and analyzed with Ethovision XT software (Noldus). Distance, time, and entries into open and closed arms were assessed.

Novel object recognition

On P66, each test mouse underwent three 10min trials: habituation (no objects), exposure to two identical inanimate objects, and then exposure to one object from trial 2 (familiar object) and a novel object that replaced the other object from trial 2. Trial 3 occurred 90min after trial 2 to assess recognition memory. All sessions were videotaped and tracked using EthoVision. Object investigation was defined as time spent sniffing the object when the nose was oriented toward the object with a <2cm nose-object distance.

Recognition memory was defined as spending significantly more time sniffing the novel object than familiar object.

Marble burying

On P70, an individual mouse was placed in a clean home cage that contained ~4cm of corncob bedding and ten blue glass marbles that were spaced out evenly in five rows. The mouse was allowed to explore the home cage for 30mins, and then photos were taken of each cage after the session was over. We utilized and modified a script from Wahl et al., (2022)[84] in ImageJ to minimize subjectivity with quantifying the amount of marbled buried.

Three-chamber sociability task

We included both social preference and social novelty in the three-chamber task, adapted from Rein et al. (2020)[85]. On P80, each test mouse underwent three consecutive 10min trials: (1) pre-test to the chamber and wire cups (no objects); (2) social preference, where one wire cup contains an inanimate object and the other contains a novel sex- and aged-matched mouse; (3) social novelty, where the mouse from trial 2 remains (familiar mouse) and a novel mouse is placed in the cup where an inanimate object was in trial 2. These three trials occurred sequentially and were videotaped and tracked using EthoVision.

Contextual fear conditioning

Contextual fear conditioning was performed in a Freezeframe Chamber (Coulbourn Instrument). Mice were fear conditioned on P88 (day 1), and the subsequent percentage

of time spent freezing was determined 24hrs later on P89 (day 2). On the day of conditioning, animals were allowed to explore the behavioral chamber for 3mins, followed by delivery of a 2sec, 0.7mA foot shock. Mice remained in the context for 15sec after the shock before returning to their home cages. Fear response was assessed 24hrs later. To determine context specificity of the conditioned response, mice trained on day 1 were placed in the same novel context as on day 1 in the same order. The novel context was created using the following stimuli: bright light, sound from a fan, peppermint scent (2 drops peppermint extract placed on paper towels below floor), and grated metal flooring. Amount of time spent frozen during a testing session of 3mins on day 2 was recorded, and quantified blinded to treatment, genotype, and sex.

Statistical analysis

Microbiome composition: For the microbiota studies, significant differences between experimental groups (α-diversity) were determined using Multiple Mann Whitney tests with two-stage step-up method of Benjamini, Krieger, and Yekutieli false discovery rate (FDR) q =1%, while differences in β-diversity were assessed using permutational multivariate analysis of variance (PERMANOVA) pairwise tests with 999 permutations Significant differences were inferred with p and q values <0.05. Significant differences in relative abundance were assessed using MaAsLin2 R package, and thresholds for significance were performed at the default setting.

Immunoblotting: Immunoblotting gels were restricted to 14 lanes after accounting for the protein ladder. Our priority objective was to determine treatment-dependent effects.

Therefore, significant differences between treatment groups (saline vs cefdinir), within sex and genotype were determined using Multiple Mann Whitney tests with two-stage step-up method of Benjamini, Krieger, and Yekutieli false discovery rate (FDR) q =1%.

Immunohistochemical quantifications: Data for EdU and Ki67 quantifications were analyzed with a two-way ANOVA with Fisher's LSD multiple comparisons test. Significance was set at $p<0.05$. Data for stereological studies were analyzed with multiple Mann Whitney tests with two-stage step-up method of Benjamini, Krieger, and Yekutieli false discovery rate (FDR) q =1%.

Bulk RNAseq: Comparisons of gene expression changes were performed using DESeq2 R package. The Wald test was used to generate p values and log2fold changes. Genes with an adjusted p value<0.05 were considered differentially expressed genes for each comparison.

Intestinal permeability: All standards and samples were assayed in triplicate wells on a 96-well plate. Data were analyzed with a two-way ANOVA with Tukey's multiple comparisons test. Significance was set at $p<0.05$.

Sera lipidome and metabolome: Datasets were analyzed ordinary two-way ANOVA with Tukey's multiple comparisons test with $p<0.05$.

Correlations and pathway analysis: Pearson correlations with linear regressions were performed between our metabolic and lipid datasets. Results with $p<0.05$ were uploaded

to MetaboAnalyst and ran through the *mus musculus* KEGG pathway library in MetaboAnalyst with the hypergeometric test for enrichment and relative-betweenness centrality as the topology measure. Enrichment metabolite sets were considered significant with an FDR<0.05.

Behavior: Datasets were analyzed using a two-way ANOVA with Tukey's multiple comparisons test, apart from a two-way repeated measures ANOVA test for the odor discrimination/habituation task.

Respective contributions

CRM, JHM, BS, MJB, and EDB contributed to conceptualization of the study. CRM performed oral gavage on all animals used for experimentation. CRM, ZG, XZ, and X-SZ dissected brain and gastrointestinal tissues for processing. CRM collected serum for metabolomic and lipid studies. CRM and AH performed the FITC-dextran assay. CRM performed immunoblotting studies. CRM, ASM, CN, KK, DT, DP, ZM, and AH performed immunohistochemistry and histology quantifications. CRM, ASM, KK, DT, CN, DP, ZM performed and analyzed behavioral studies. CRM, ZG and JX contributed to data analysis. CRM wrote the manuscript, EDB revised initial drafts, EDB, MJB, JHM, BS, JX, JA, and STV revised the final version.

Acknowledgements

These studies were supported by NIH TL1TR003019, NJGOV CAUT22AFP011, NIH NINDS 1F99NS130926 to CRM; Autism Research Institute, NJHF PC 124-22, Busch Biomedical Grant, Lurie Family Foundation, Mindworks Charitable Lead Trust to

EDB; Emch Fund for Microbial Diversity, C&D Fund to MJB. We would like to thank the Rutgers Cancer Institute Metabolomics Shared Resource core facility led by Dr. Xiaoyang Su, with assistance from Eric Chiles and Dr. Maria Elena Diaz Rubio. Figures created with BioRender are specified in the corresponding figure legends.

References

1. CDC. Outpatient Clinical Care for Pediatric Populations. *Antibiotic Prescribing and Use* https://www.cdc.gov/antibiotic-use/hcp/clinical-care/pediatric-outpatient.html (2024).
2. Donovan, B. M. *et al.* Dose, Timing, and Type of Infant Antibiotic Use and the Risk of Childhood Asthma. *Clin Infect Dis* **70**, 1658–1665 (2020).
3. Aversa, Z. *et al.* Association of Infant Antibiotic Exposure With Childhood Health Outcomes. *Mayo Clinic Proceedings* **96**, 66–77 (2021).
4. Wimberley, T. *et al.* Otitis media, antibiotics, and risk of autism spectrum disorder. *Autism Res* **11**, 1432–1440 (2018).
5. Lavebratt, C. *et al.* Early exposure to antibiotic drugs and risk for psychiatric disorders: a population-based study. *Transl Psychiatry* **9**, 1–12 (2019).
6. Slykerman, R. F. *et al.* Exposure to antibiotics in the first 24 months of life and neurocognitive outcomes at 11 years of age. *Psychopharmacology* **236**, 1573–1582 (2019).
7. Volkova, A. *et al.* Effects of early-life penicillin exposure on the gut microbiome and frontal cortex and amygdala gene expression. *iScience* **24**, 102797 (2021).
8. Hsiao, E. Y. *et al.* Microbiota Modulate Behavioral and Physiological Abnormalities Associated with Neurodevelopmental Disorders. *Cell* **155**, 1451–1463 (2013).
9. Vuong, H. E. *et al.* The maternal microbiome modulates fetal neurodevelopment in mice. *Nature* **586**, 281–286 (2020).

10. Neufeld, K.-A. M., Kang, N., Bienenstock, J. & Foster, J. A. Effects of intestinal microbiota on anxiety-like behavior. *Commun Integr Biol* **4**, 492–494 (2011).

11. Leclercq, S. *et al.* Low-dose penicillin in early life induces long-term changes in murine gut microbiota, brain cytokines and behavior. *Nat Commun* **8**, 15062 (2017).

12. Yassour, M. *et al.* Natural history of the infant gut microbiome and impact of antibiotic treatment on bacterial strain diversity and stability. *Sci. Transl. Med.* **8**, 343ra81 (2016).

13. Ruiz, V. E. *et al.* A single early-in-life macrolide course has lasting effects on murine microbial network topology and immunity. *Nat Commun* **8**, 518 (2017).

14. Jernberg, C., Löfmark, S., Edlund, C. & Jansson, J. K. Long-term ecological impacts of antibiotic administration on the human intestinal microbiota. *The ISME Journal* **1**, 56–66 (2007).

15. Chernikova, M. A. *et al.* The Brain-Gut-Microbiome System: Pathways and Implications for Autism Spectrum Disorder. *Nutrients* **13**, 4497 (2021).

16. Agirman, G. & Hsiao, E. Y. SnapShot: The microbiota-gut-brain axis. *Cell* **184**, 2524-2524.e1 (2021).

17. Cryan, J. F. *et al.* The Microbiota-Gut-Brain Axis. *Physiol Rev* **99**, 1877–2013 (2019).

18. Osman, A. *et al.* Acetate supplementation rescues social deficits and alters transcriptional regulation in prefrontal cortex of *Shank3* deficient mice. *Brain, Behavior, and Immunity* **114**, 311–324 (2023).

19. Desbonnet, L., Clarke, G., Shanahan, F., Dinan, T. G. & Cryan, J. F. Microbiota is essential for social development in the mouse. *Molecular Psychiatry* **19**, 146–148 (2014).

20. Möhle, L. *et al.* Ly6C(hi) Monocytes Provide a Link between Antibiotic-Induced Changes in Gut Microbiota and Adult Hippocampal Neurogenesis. *Cell Rep* **15**, 1945–1956 (2016).

21. Chu, C. *et al.* The microbiota regulate neuronal function and fear extinction learning. *Nature* **574**, 543–548 (2019).

22. Hofford, R. S. *et al.* Microbiome depletion increases fentanyl self-administration and alters the striatal proteome through short-chain fatty acids. *eNeuro* **11** ENEURO.0388-23.2023 (2023)
23. Cruz-Pereira, J. S. *et al.* Age-associated deficits in social behaviour are microbiota-dependent. *Brain Behav Immun* **110**, 119–124 (2023).
24. DiCicco-Bloom, E. & McDermott, C. R. Neural Development and Neurogenesis. in *Kaplan and Sadock's Comprehensive Textbook of Psychiatry* vol. 1 53–67 (Wolters Kluwer).
25. Connacher, R. J., DiCicco-Bloom, E. & Millonig, J. H. Using Human Induced Neural Precursor Cells to Define Early Neurodevelopmental Defects in Syndromic and Idiopathic Autism. *Curr Pharmacol Rep* **4**, 422–435 (2018).
26. Kempermann, G., Song, H. & Gage, F. H. Neurogenesis in the Adult Hippocampus. *Cold Spring Harb Perspect Biol* **7**, a018812 (2015).
27. Greco, C. M. *et al.* Neuropathologic features in the hippocampus and cerebellum of three older men with fragile X syndrome. *Mol Autism* **2**, 2 (2011).
28. Obiorah, M., McCandlish, E., Buckley, B. & DiCicco-Bloom, E. Hippocampal developmental vulnerability to methylmercury extends into prepubescence. *Front Neurosci* **9**, 150 (2015).
29. Falluel-Morel, A. *et al.* Developmental mercury exposure elicits acute hippocampal cell death, reductions in neurogenesis, and severe learning deficits during puberty. *J Neurochem* **103**, 1968–1981 (2007).
30. Horev, G. *et al.* Dosage-dependent phenotypes in models of 16p11.2 lesions found in autism. *Proc Natl Acad Sci U S A* **108**, 17076–17081 (2011).
31. Portmann, T. *et al.* Behavioral Abnormalities and Circuit Defects in the Basal Ganglia of a Mouse Model of 16p11.2 Deletion Syndrome. *Cell Reports* **7**, 1077–1092 (2014).
32. Pucilowska, J. *et al.* Pharmacological Inhibition of ERK Signaling Rescues Pathophysiology and Behavioral Phenotype Associated with 16p11.2 Chromosomal Deletion in Mice. *J. Neurosci.* **38**, 6640–6652 (2018).

33. Kim, J. *et al.* Dissecting 16p11.2 hemi-deletion to study sex-specific striatal phenotypes of neurodevelopmental disorders. *Mol Psychiatry* **29**, 1310-1321 (2024).

34. Pucilowska, J. *et al.* The 16p11.2 Deletion Mouse Model of Autism Exhibits Altered Cortical Progenitor Proliferation and Brain Cytoarchitecture Linked to the ERK MAPK Pathway. *Journal of Neuroscience* **35**, 3190–3200 (2015).

35. Béland-Millar, A. *et al.* 16p11.2 haploinsufficiency reduces mitochondrial biogenesis in brain endothelial cells and alters brain metabolism in adult mice. *Cell Reports* **42**, 112485. (2023).

36. Menzies, C. *et al.* Distinct Basal Metabolism in Three Mouse Models of Neurodevelopmental Disorders. *eNeuro* **8**, ENEURO.0292-20.2021 (2021).

37. Qureshi, A. Y. *et al.* Opposing Brain Differences in 16p11.2 Deletion and Duplication Carriers. *J Neurosci* **34**, 11199–11211 (2014).

38. Weiss, L. A. *et al.* Association between microdeletion and microduplication at 16p11.2 and autism. *N Engl J Med* **358**, 667–675 (2008).

39. Niarchou, M. *et al.* Psychiatric disorders in children with 16p11.2 deletion and duplication. *Transl Psychiatry* **9**, 8 (2019).

40. Weiner, D. J. *et al.* Statistical and functional convergence of common and rare genetic influences on autism at chromosome 16p. *Nat Genet* **54**, 1630–1639 (2022).

41. Brown, E. M., Clardy, J. & Xavier, R. J. Gut microbiome lipid metabolism and its impact on host physiology. *Cell Host Microbe* **31**, 173–186 (2023).

42. Tomasello, D. L. *et al.* 16pdel lipid changes in iPSC-derived neurons and function of FAM57B in lipid metabolism and synaptogenesis. *iScience* **25**, 103551 (2022).

43. Mallick, H. *et al.* Multivariable association discovery in population-scale meta-omics studies. *PLOS Computational Biology* **17**, e1009442 (2021).

44. Bond, A. M. *et al.* Differential Timing and Coordination of Neurogenesis and Astrogenesis in Developing Mouse Hippocampal Subregions. *Brain Sciences* **10**, 909 (2020).

45. Bond, A. M., Ming, G.-L. & Song, H. Ontogeny of adult neural stem cells in the mammalian brain. *Curr Top Dev Biol* **142**, 67–98 (2021).

46. Abrahams, B. S. *et al.* SFARI Gene 2.0: a community-driven knowledgebase for the autism spectrum disorders (ASDs). *Mol Autism* **4**, 36 (2013).

47. Fu, J. M. *et al.* Rare coding variation provides insight into the genetic architecture and phenotypic context of autism. *Nat Genet* **54**, 1320–1331 (2022).

48. Xia, J., Psychogios, N., Young, N. & Wishart, D. S. MetaboAnalyst: a web server for metabolomic data analysis and interpretation. *Nucleic Acids Res* **37**, W652–W660 (2009).

49. Bakirtzis, C., Smyrni, N., Afrantou, T., Boziki, M. K. & Grigoriadis, N. Spastic gait, intellectual disability and seizures due to a rare mutation causing hyperargininemia. *Clin Neurol Neurosurg* **208**, 106895 (2021).

50. Diaz, G. A., Bechter, M. & Cederbaum, S. D. The role and control of arginine levels in arginase 1 deficiency. *J Inherit Metab Dis* **46**, 3–14 (2023).

51. Liang, W. *et al.* Alterations Of Glycerophospholipid And Fatty Acyl Metabolism In Multiple Brain Regions Of Schizophrenia Microbiota Recipient Mice. *Neuropsychiatr Dis Treat* **15**, 3219–3229 (2019).

52. Liu, P. *et al.* Altered brain arginine metabolism in schizophrenia. *Transl Psychiatry* **6**, e871(2016).

53. Xu, S. *et al.* Spatially and temporally probing distinctive glycerophospholipid alterations in Alzheimer's disease mouse brain via high-resolution ion mobility-enabled sn-position resolved lipidomics. *Nat Commun* **15**, 6252 (2024).

54. Blaser, M. J. Antibiotic use and its consequences for the normal microbiome. *Science* **352**, 544–545 (2016).

55. Bokulich, N. A. *et al.* Antibiotics, birth mode, and diet shape microbiome maturation during early life. *Sci. Transl. Med.* **8**, 343ra82 (2016).

56. Oliphant, K. *et al.* Bacteroidota and Lachnospiraceae integration into the gut microbiome at key time points in early life are linked to infant neurodevelopment. *Gut Microbes* **13**, 1997560 (2021).

57. Sugino, K. Y., Ma, T., Paneth, N. & Comstock, S. S. Effect of Environmental Exposures on the Gut Microbiota from Early Infancy to Two Years of Age. *Microorganisms* **9**, 2140 (2021).

58. Bourassa, M. W., Alim, I., Bultman, S. J. & Ratan, R. R. Butyrate, neuroepigenetics and the gut microbiome: Can a high fiber diet improve brain health? *Neurosci Lett* **625**, 56–63 (2016).

59. Lach, G. *et al.* Enduring neurobehavioral effects induced by microbiota depletion during the adolescent period. *Transl Psychiatry* **10**, 1–16 (2020).

60. Calegari, F., Haubensak, W., Haffner, C. & Huttner, W. B. Selective Lengthening of the Cell Cycle in the Neurogenic Subpopulation of Neural Progenitor Cells during Mouse Brain Development. *J. Neurosci.* **25**, 6533–6538 (2005).

61. Vega, C. J. & Peterson, D. A. Stem cell proliferative history in tissue revealed by temporal halogenated thymidine analog discrimination. *Nat Methods* **2**, 167–169 (2005).

62. Mairet-Coello, G., Tury, A. & DiCicco-Bloom, E. Insulin-like growth factor-1 promotes G(1)/S cell cycle progression through bidirectional regulation of cyclins and cyclin-dependent kinase inhibitors via the phosphatidylinositol 3-kinase/Akt pathway in developing rat cerebral cortex. *J Neurosci* **29**, 775–788 (2009).

63. Li, H., Gao, J. & Zhang, S. Functional and Clinical Characteristics of Cell Adhesion Molecule CADM1 in Cancer. *Front Cell Dev Biol* **9**, 714298 (2021).

64. Majdzadeh, N. *et al.* HDAC4 inhibits cell cycle progression and protects neurons from cell death. *Dev Neurobiol* **68**, 1076–1092 (2008).

65. Lin, J., de Rezende, V. L., de Aguiar da Costa, M., de Oliveira, J. & Gonçalves, C. L. Cholesterol metabolism pathway in autism spectrum disorder: From animal models to clinical observations. *Pharmacol Biochem Behav* **223**, 173522 (2023).

66. Orth, M. & Bellosta, S. Cholesterol: its regulation and role in central nervous system disorders. *Cholesterol* **2012**, 292598 (2012).

67. Cartocci, V. *et al.* Altered Brain Cholesterol/Isoprenoid Metabolism in a Rat Model of Autism Spectrum Disorders. *Neuroscience* **372**, 27–37 (2018).

68. Walters, R. G. *et al.* A novel highly-penetrant form of obesity due to microdeletions on chromosome 16p11.2. *Nature* **463**, 671–675 (2010).

69. Jacquemont, S. *et al.* Mirror extreme BMI phenotypes associated with gene dosage at the chromosome 16p11.2 locus. *Nature* **478**, 97–102 (2011).

70. Knowles, R. G., Palacios, M., Palmer, R. M. & Moncada, S. Formation of nitric oxide from L-arginine in the central nervous system: a transduction mechanism for stimulation of the soluble guanylate cyclase. *Proc Natl Acad Sci U S A* **86**, 5159–5162 (1989).

71. Lourenço, C. F. & Laranjinha, J. Nitric Oxide Pathways in Neurovascular Coupling Under Normal and Stress Conditions in the Brain: Strategies to Rescue Aberrant Coupling and Improve Cerebral Blood Flow. *Front Physiol* **12**, 729201 (2021).

72. Yoon, J. H. *et al.* Brain lipidomics: From functional landscape to clinical significance. *Science Advances* **8**, eadc9317 (2022).

73. Zheng, P. *et al.* The gut microbiome modulates gut-brain axis glycerophospholipid metabolism in a region-specific manner in a nonhuman primate model of depression. *Mol Psychiatry* **26**, 2380–2392 (2021).

74. Chen, J.-J. *et al.* Absence of gut microbiota affects lipid metabolism in the prefrontal cortex of mice. *Neurol Res* **41**, 1104–1112 (2019).

75. Bolyen, E. *et al.* Reproducible, interactive, scalable and extensible microbiome data science using QIIME 2. *Nat Biotechnol* **37**, 852–857 (2019).

76. Callahan, B. J. *et al.* DADA2: High-resolution sample inference from Illumina amplicon data. *Nat Methods* **13**, 581–583 (2016).

77. Pruesse, E. *et al.* SILVA: a comprehensive online resource for quality checked and aligned ribosomal RNA sequence data compatible with ARB. *Nucleic Acids Res* **35**, 7188–7196 (2007).

78. Poillet-Perez, L. *et al.* Autophagy maintains tumour growth through circulating arginine. *Nature* **563**, 569–573 (2018).

79. Su, X. *et al.* In-Source CID Ramping and Covariant Ion Analysis of Hydrophilic Interaction Chromatography Metabolomics. *Anal Chem* **92**, 4829–4837 (2020).

80. Tsugawa, H. *et al.* MS-DIAL: data-independent MS/MS deconvolution for comprehensive metabolome analysis. *Nat Methods* **12**, 523–526 (2015).

81. Melamud, E., Vastag, L. & Rabinowitz, J. D. Metabolomic analysis and visualization engine for LC-MS data. *Anal Chem* **82**, 9818–9826 (2010).

82. Chen, L. *et al.* Metabolite discovery through global annotation of untargeted metabolomics data. *Nat Methods* **18**, 1377–1385 (2021).

83. Allen Institute for Brain Science. Allen Mouse Brain Atlas. (2004).

84. Wahl, L. *et al.* A Novel Automated Approach for Improving Standardization of the Marble Burying Test Enables Quantification of Burying Bouts and Activity Characteristics. *eNeuro* **9**, ENEURO.0446-21.2022. (2022).

85. Rein, B., Ma, K. & Yan, Z. A Standardized Social Preference Protocol for Measuring Social Deficits in Mouse Models of Autism. *Nat Protoc* **15**, 3464–3477 (2020).

Main figures

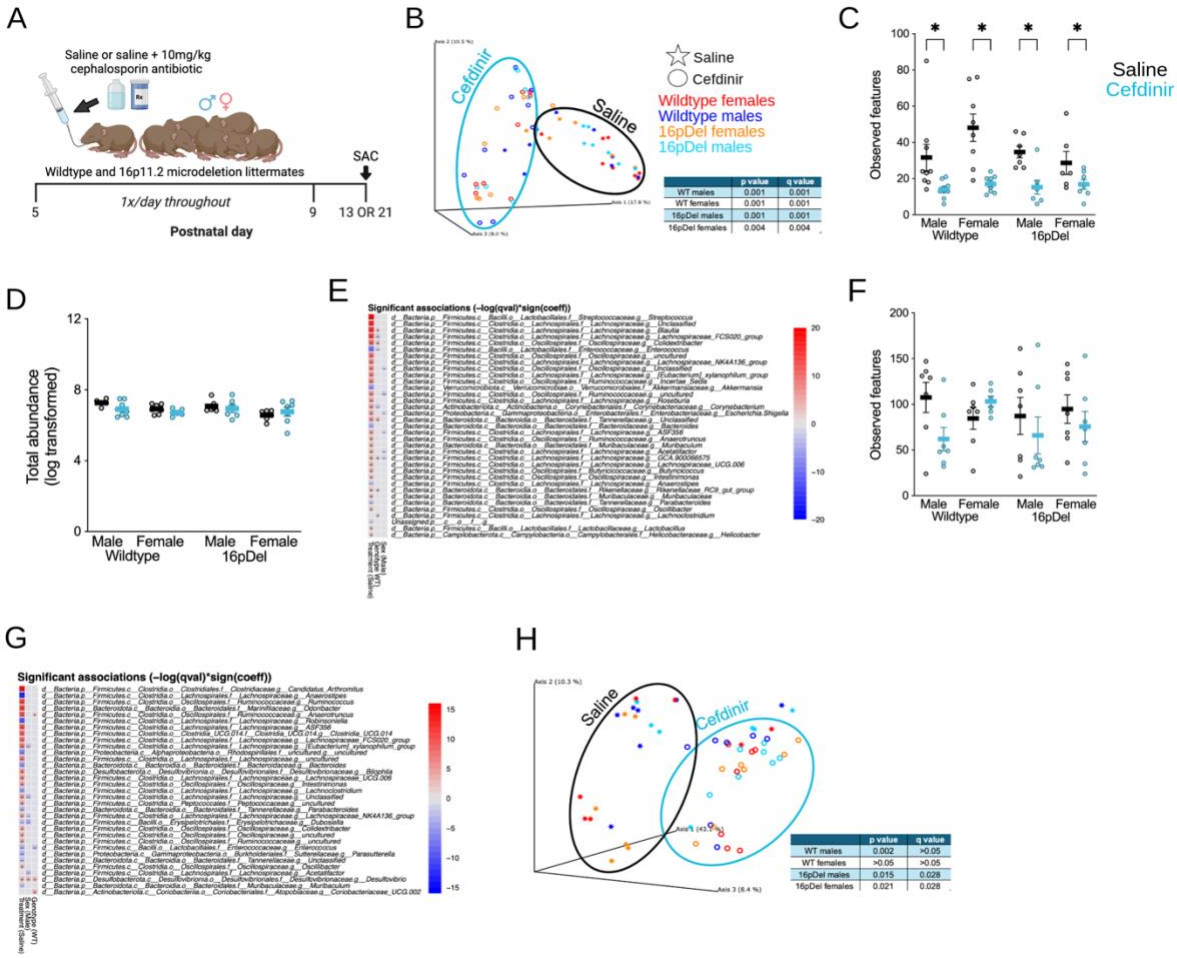

Figure 1: Early-life cefdinir exposure successfully perturbed the gut microbiome.
a Litters comprised of ~50:50 ratios of WT and 16pDel pups were randomly assigned to receive saline or 10mg/kg cefdinir via oral gavage on P5-9. Offspring were then sacrificed on P13 or P21 for experimentation. 4 litters/treatment. **b** Principal coordinate analysis (PCoA) plot depicting Jaccard distances of each cecal microbiota sample at P13. **c** Early-life cefdinir exposure decreased the number of relative bacterial taxa at the genus level in P13 cecal samples. **d** Log transformed values of total bacterial abundance was comparable between saline- and cefdinir-exposed cecal samples. **e** A heatmap of the top taxa that differed in relative abundances across treatment, genotype, and sex at P13. Red represents depleted bacteria and blue represents sustained bacteria. Color intensity depicts the strength of the association. **f** There are no changes in α-diversity in P21 cecal samples. **g** A heatmap of the top taxa that differed in relative abundances across treatment, genotype, and sex at P21. **h** PCoA plot depicting Jaccard distances of each cecal microbiota sample at P21. Comparisons for **b, h** were assessed using permutational multivariate analysis of variance (PERMANOVA) pairwise tests with 999 permutations. Significant differences were inferred with p and q values <0.05, provided in the tables. Comparisons for **c-d, f** were made using Multiple Mann Whitney tests with two-stage step-up method of Benjamini, Krieger, and Yekutieli false discovery rate (FDR) q =1%. Data are represented as Mean ± SEM, *q<0.05. Significance for **e,g** was inferred by MaAsLin2 analysis using Log10 taxon. For detailed N values see Supplementary file 1. Figure 1A was created with BioRender.

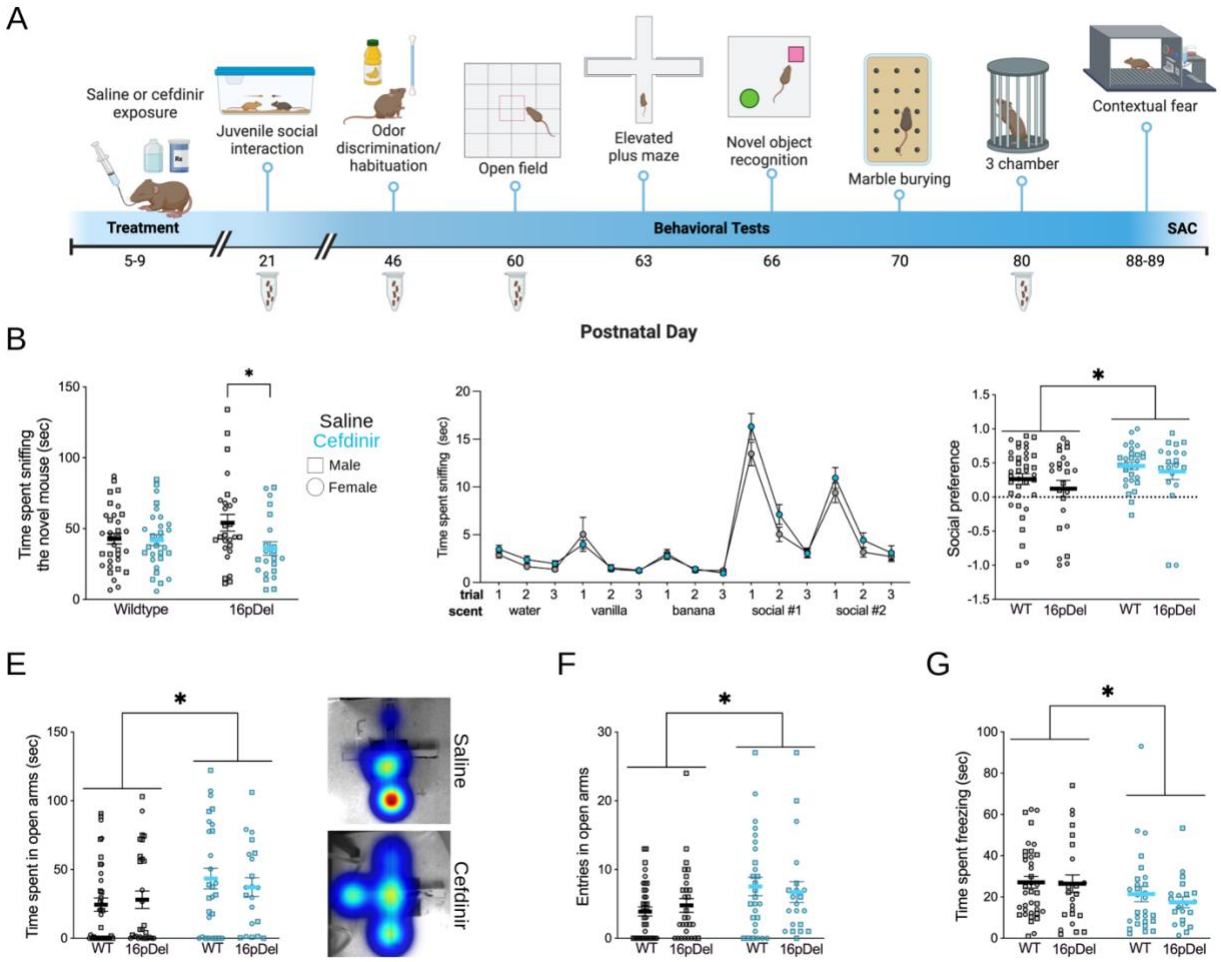

Figure 2: Cefdinir-exposed mice display altered behavioral outcomes throughout the lifespan.

a Litters were randomly assigned to receive saline or 10mg/kg cefdinir via oral gavage on P5-9. Offspring then underwent a longitudinal behavioral paradigm from P21-P89. **b** Juvenile cefdinir-exposed mice were less social than saline-exposed mice, which was driven by the 16pDel group. Two-way ANOVA main effect of treatment: $F(1, 107) = 4.312$, $p=0.0402$. Tukey's multiple comparisons test 16pDel:Saline vs.16pDel:Cefdinir adjusted $p=0.0491$. **c** There was no difference in social odor detection and discrimination between saline- and cefdinir-exposed mice using a two-way repeated measures ANOVA. **d** Cefdinir-exposed mice displayed an increase in social preference compared to saline-exposed mice, $F(1, 106) = 5.610$, $p=0.0197$, two-way ANOVA. The social preference index was calculated as the difference between time spent with the mouse and the inanimate object divided by the sum of the time spent with the mouse and the inanimate object. A positive score indicates increased preference for the mouse (more social) where a negative score indicates increased preference for the inanimate object (antisocial). **e-f** Cefdinir-exposed mice displayed less risk-aversion behaviors, indicated by **e** increased time $F(1, 111) = 4.806$, $p=0.0305$, and **f** entries in the open arms of the elevated plus maze $F(1, 111) = 6.360$, $p=0.0131$ using a two-way ANOVA. **g** Cefdinir-exposed mice froze less in the 24hr contextual fear extinction trial, indicating compromised associative learning abilities, $F(1, 106) = 4.408$, $p=0.0381$, two-way ANOVA. All data are represented as Mean ± SEM. For detailed N values see Supplementary file 1. Figure 2A was created with BioRender.

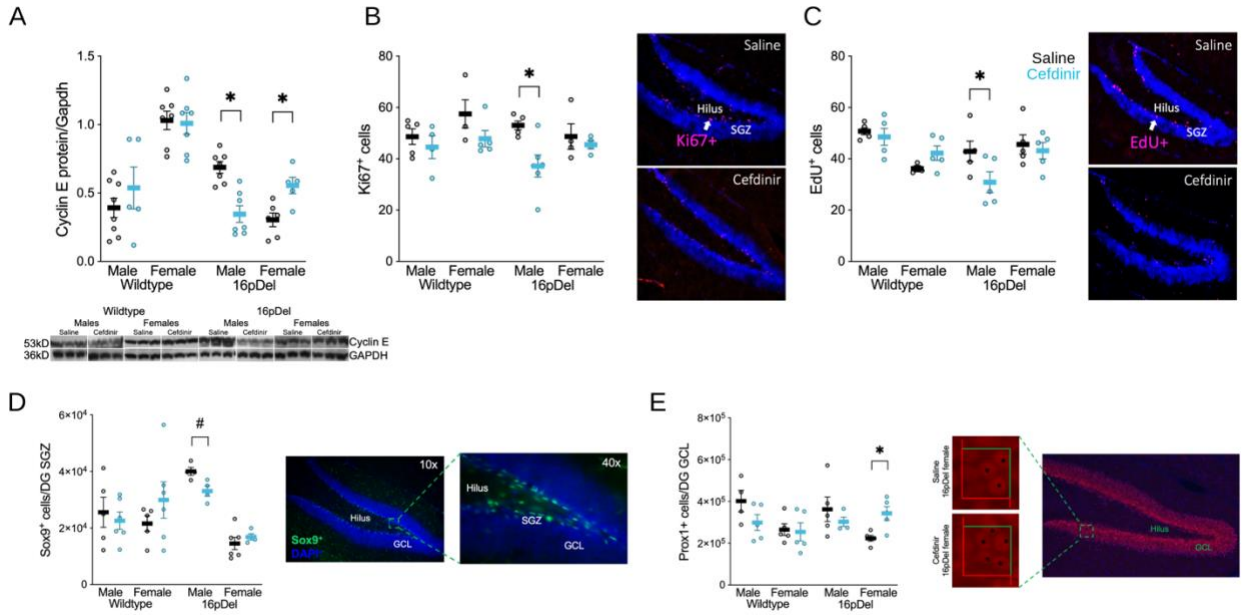

Figure 3: Cefdinir exposure alters hippocampal development in genotype- and sex-dependent fashion.

a Western blot of cyclin E protein normalized to GAPDH of individual 35ug hippocampal lysates from P13 mice. A total of 4 membranes were used, where each membrane contained 5-8 mice/treatment within the same genotype and sex. Thus, only treatment comparisons could be made from these data. Representative bands of a subset of mice from each group are provided. **b-c** P13 cefdinir-exposed 16pDel mice displayed reduced numbers of **b** $Ki67^+$ and **c** EdU^+ cells in the hilus and subgranular zone of the hippocampal dentate gyrus. Cells were visualized by immunofluorescence and the total number of positive cells was quantified on an average of 8 sections/mouse across 4 litters/treatment. Representative images from a saline- and cefdinir-exposed 16pDel male are provided. **d** P21 cefdinir-exposed 16pDel males had a trending decrease in numbers of $Sox9^+$ cells in the subgranular zone. **e** P21 cefdinir-exposed 16pDel females had increased numbers of $Prox1^+$ granule cell neurons in the granule cell layer. Representative images are provided. Comparisons for **a** was assessed using Multiple Mann Whitney tests with two-stage step-up method of Benjamini, Krieger, and Yekutieli false discovery rate (FDR) q =1%. *q<0.05, **q<0.01. Comparisons for **b-c** were made using a two-way ANOVA with Fisher's LSD, *p<0.05. Comparisons for stereology datasets **d-e** were made using Multiple Mann Whitney tests with two-stage step-up method of Benjamini, Krieger, and Yekutieli false discovery rate (FDR) q =1%. *p<0.05, $^{\#}p$<0.06. All data are represented as Mean ± SEM. For detailed N values see Supplementary file 1.

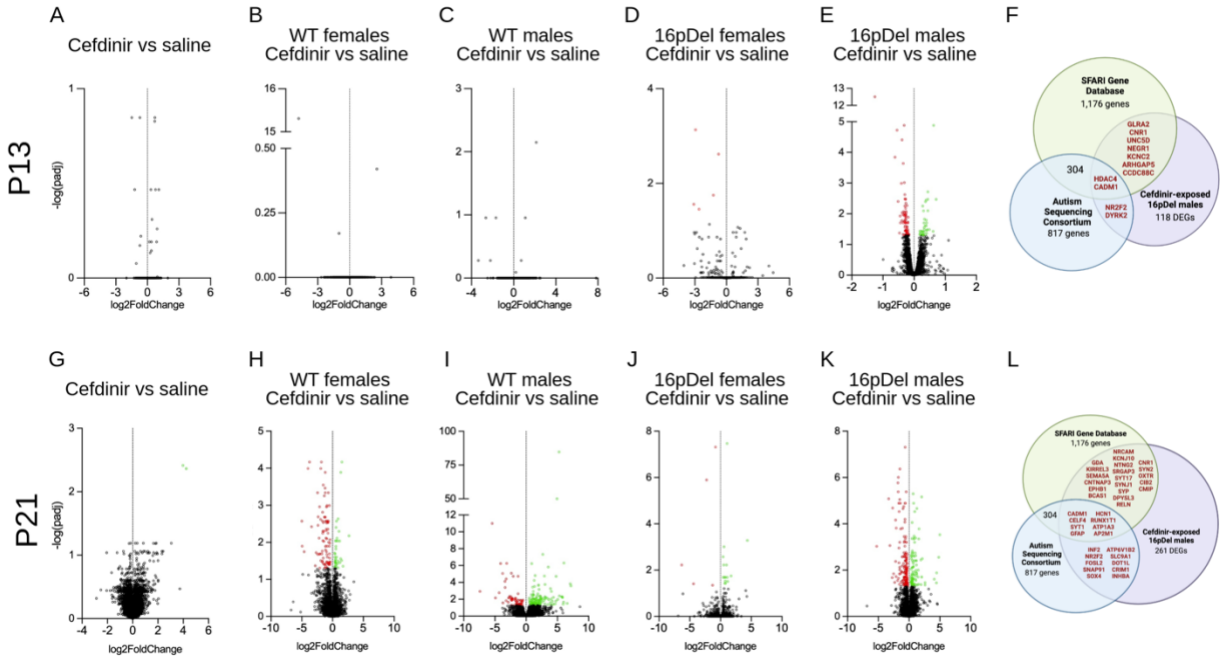

Figure 4: Differentially expressed genes in cefdinir-exposed 16pDel males overlap with human autism risk genes.

Mice were sacrificed on P13 or P21 and one hemisphere of the hippocampus was randomly selected and analyzed using bulk RNA sequencing. **a-e** Volcano plots depicting differentially expressed genes (DEGs) across **a** all cefdinir-exposed mice or stratified by sex and genotype: **b** WT females **c** WT males **d** 16pDel females and **e** 16pDel males at P13. **f** Venn diagram depicting overlap between 11 DEGs of cefdinir exposed 16pDel male mice (purple) with known ASD genes reported in the SFARI (green) and ASC (blue) databases. **g-k** Volcano plots depicting DEGs across **g** all cefdinir-exposed mice or stratified by sex and genotype: **h** WT females **i** WT males **j** 16pDel females and **k** 16pDel males at P21. **l** Venn diagram depicting overlap between 38 DEGs of cefdinir exposed 16pDel male mice (purple) with known ASD genes reported in the SFARI (green) and ASC (blue). DEGs were detected using the DeSeq2 package in R. The Wald test was used to generate p-values and log2fold changes. Given the exploratory design of this study and small sample size (n=3 mice/group, across 3 litters/treatment), significance was assessed with a padj<0.05 only, as applying the standard log2fold cutoff of <-1 or >1 in addition to padj<0.05 did not yield significance DEGs across treatment comparisons. Upregulated genes are depicted in green and downregulated genes are depicted in red. DEGs with a padj>0.05 are depicted in black. For detailed N values see Supplementary file 1. Figures 4F and 4L were created with BioRender.

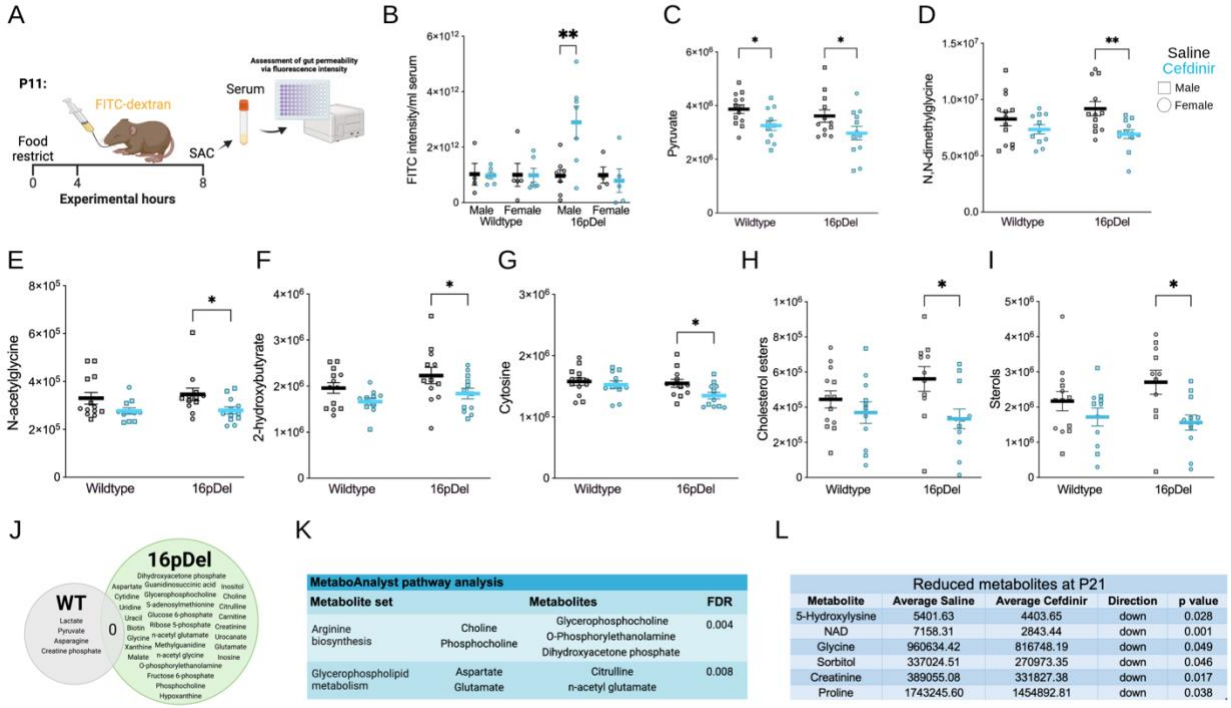

MetaboAnalyst pathway analysis			
Metabolite set	Metabolites		FDR
Arginine biosynthesis	Choline Phosphocholine	Glycerophosphocholine O-Phosphorylethanolamine Dihydroxyacetone phosphate	0.004
Glycerophospholipid metabolism	Aspartate Glutamate	Citrulline n-acetyl glutamate	0.008

Reduced metabolites at P21				
Metabolite	Average Saline	Average Cefdinir	Direction	p value
5-Hydroxylysine	5401.63	4403.65	down	0.028
NAD	7158.31	2843.44	down	0.001
Glycine	960634.42	816748.19	down	0.049
Sorbitol	337024.51	270973.35	down	0.046
Creatinine	389055.08	331827.38	down	0.017
Proline	1743245.60	1454892.81	down	0.038

Figure 5: Distinct intestinal permeability and metabolic profiles in cefdinir-exposed 16pDel mice. a Experimental design for FITC-dextran studies. On P11, mice from 6 litters/treatment were fasted 4 hours before gavage of FITC-dextran. An additional 4 hours later, offspring were anesthetized, and serum was collected and assessed for fluorescence intensity. **b** A three-fold increase in FITC intensity was observed in cefdinir-exposed 16pDel male mice using an Ordinary two-way ANOVA $F(1, 36) = 2.865$, $p=0.0992$ and Tukey's multiple comparisons test 16pDel:Saline vs. 16pDel:Cefdinir adjusted **$p=0.0037$. **c-i** Peak intensity values of select metabolites and lipids at P13 that were reduced following cefdinir exposure. All data were analyzed using an Ordinary two-way ANOVA with Tukey's multiple comparisons test. All data are represented as Mean ± SEM, *$p<0.05$. **c** Pyruvate $F(1, 44) = 8.762$, $p=0.0049$, **d** N,N-dimethylglycine $F(1, 44) = 8.928$, $p=0.0046$ with Tukey's multiple comparisons test 16pDel:Saline vs. 16pDel:Cefdinir adjusted $p=0.0044$, **e** N-acetylglycine $F(1, 44) = 8.137$, $p=0.0066$ with Tukey's multiple comparisons test 16pDel:Saline vs. 16pDel:Cefdinir adjusted $p=0.0294$. **f** 2-hydroxybutyrate $F(1, 44) = 7.012$, $p=0.0112$ with Tukey's multiple comparisons test 16pDel:Saline vs. 16pDel:Cefdinir adjusted $p=0.0377$. **g** Cytosine $F(1, 44) = 4.223$, $p=0.0458$ with Tukey's multiple comparisons test 16pDel:Saline vs. 16pDel:Cefdinir adjusted $p=0.0254$. **h** Cholesterol esters $F(1, 43) = 6.599$, $p=0.0138$ with Tukey's multiple comparisons test 16pDel:Saline vs. 16pDel:Cefdinir adjusted $p=0.0460$. **i** Sterols $F(1, 43) = 8.439$, $p=0.0058$. Tukey's multiple comparisons test 16pDel:Saline vs. 16pDel:Cefdinir adjusted $p=0.0271$. **j** Venn diagram displaying metabolites that were correlated with cholesterol ester content in cefdinir-exposed WT or 16pDel mice. **k** A table displaying the enriched metabolite sets on the 29 correlated metabolites in cefdinir-exposed 16pDel mice. Analyses were performed using the *mus musculus* KEGG pathway library in MetaboAnalyst with the hypergeometric test for enrichment and relative-betweenness centrality as the topology measure. **l** Table displaying the metabolites that were reduced in cefdinir-exposed mice at P21. For detailed N values see Supplementary file 1. Figures 5A, 5J, and 5K were created with BioRender.